iScience

CellPress
OPEN ACCESS

Article

Anomalous and colossal thermal expansion, photoluminescence, and dielectric properties in lead halide-layered perovskites with cyclohexylammonium and cyclopentylammonium cations

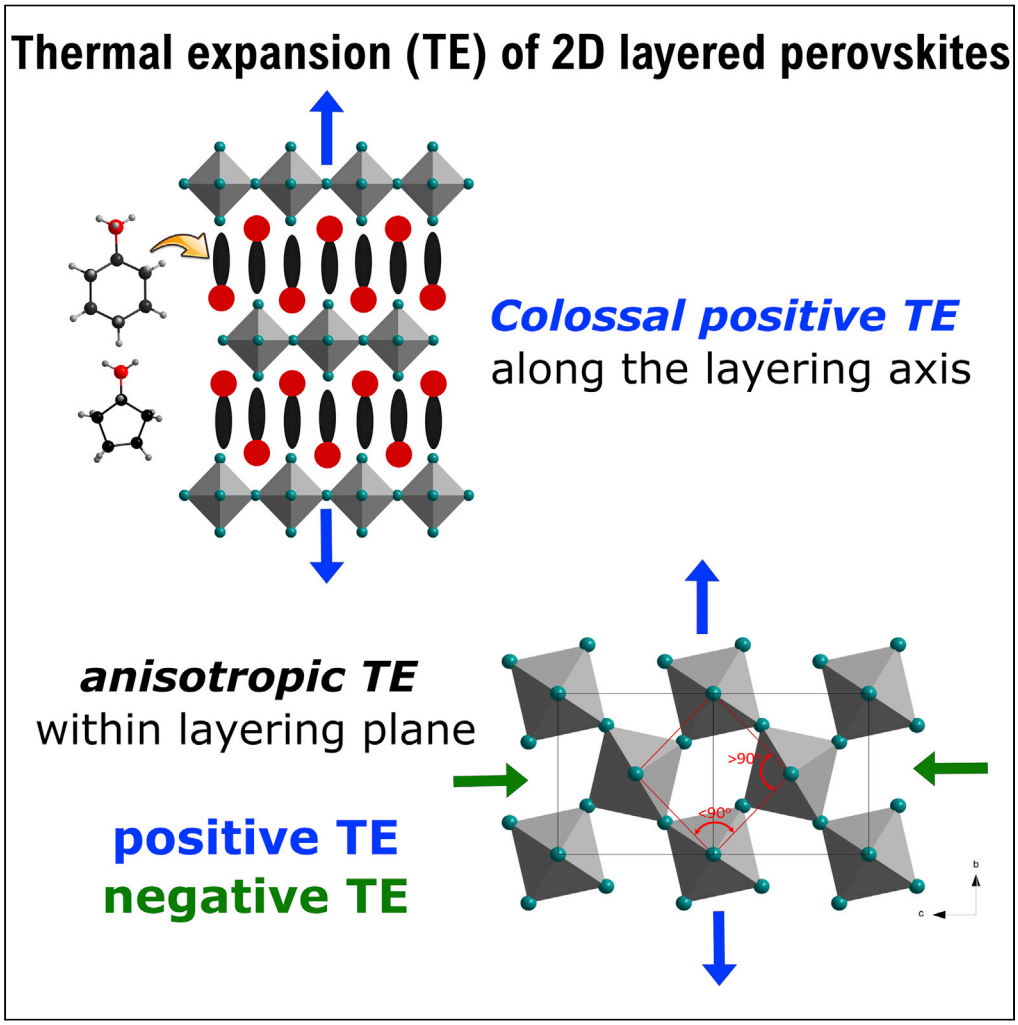

Alberto Cuquejo-Cid, Alberto García-Fernández, Catalin Popescu, ..., Socorro Castro-García, Digna Vázquez-García, Manuel Sánchez-Andújar

alberto.garcia.fernandez@udc.es (A.G.-F.)
m.andujar@udc.es (M.S.-A.)

Highlights

2D lead halide layered perovskites exhibit multiple phase and dielectric transitions

These compounds show an anisotropic and unconventional thermal expansion (TE)

Colossal positive TE along the layering axis because of dynamic motion of cations

Negative TE and colossal PTE within layering planes related to a wine-rack effect

Cuquejo-Cid et al., iScience 25, 104450
June 17, 2022
https://doi.org/10.1016/j.isci.2022.104450

iScience

CellPress
OPEN ACCESS

Article

Anomalous and colossal thermal expansion, photoluminescence, and dielectric properties in lead halide-layered perovskites with cyclohexylammonium and cyclopentylammonium cations

Alberto Cuquejo-Cid,[1] Alberto García-Fernández,[1,2,*] Catalin Popescu,[3] Juan Manuel Bermúdez-García,[1] María A. Señarís-Rodríguez,[1] Socorro Castro-García,[1] Digna Vázquez-García,[1] and Manuel Sánchez-Andújar[1,4,*]

SUMMARY

A detailed study of lead halide-layered perovskites with general formula A_2PbX_4 (where A is cyclohexylammonium (CHA) or cyclopentylammonium (CPA) cation and X is Cl^- or Br^- anion) is presented. Using variable temperature synchrotron X-ray powder diffraction, we observe that these compounds exhibit diverse crystal structures above room temperature. Very interestingly, we report some unconventional thermomechanical responses such as uniaxial negative thermal expansion and colossal positive thermal expansion in a perpendicular direction. For the polymorphs of $(CHA)_2PbBr_4$, the volumetric thermal expansion coefficient is among the highest reported for any extended inorganic crystalline solid, reaching 480 MK^{-1}. The phase transitions are confirmed by calorimetry and dielectric measurements, where the dielectric versus temperature curves show anomalies related with the order-disorder phase transitions. In addition, these compounds exhibit a broad photoluminescence (PL) emission with a large Stokes shift, which is related with an exciton PL emission.

INTRODUCTION

Along the last decade, hybrid organic-inorganic halides with perovskite and related structures have been established as promising semiconducting materials with excellent optoelectronic applications, such as photovoltaics (Kojima et al., 2009; Tsai et al., 2016), light-emitting diodes (LEDs) (Tan et al., 2014), photodetectors (Dou et al., 2014), field-effect diodes, etc. In addition to their exceptional and unprecedented optoelectronic properties, hybrid halide perovskites are synthesized by easy and low-cost solution-based processes (Chen et al., 2015).

Beyond their optoelectronics properties, hybrid halide perovskites and related structures also exhibit interesting properties, such as ferroelectricity (Pandey et al., 2019), ferroelasticity (Bari et al., 2020), weak ferromagnetism (Bandyopadhyay et al., 2020), and ionic conductivity (Senocrate and Maier, 2019) among others.

Recently, two-dimensional (2D) hybrid-layered perovskites have emerged from the shadows of three-dimensional (3D) perovskites because of their higher chemical stability and the large variety of organic cations that can be included in their composition, as well as their interesting functional and multifunctional properties (Mao et al., 2019; Zhang et al., 2020).

The interest on 2D perovskites began toward the end of the 20th century when different types of 2D materials with large variety of organic cations were synthesized by Mitzi (Mitzi, 2007) and other research groups (Papavassiliou and Koutselas, 1995; Zhu et al., 2002). More recently, layered perovskites have been revisited because of their interesting photoluminescence (PL) properties (Mao et al., 2019; Pedesseau et al., 2016; Smith et al., 2019), ferroelectricity (Chen et al., 2020), and even photovoltaic performance by edge oriented layers (Tsai et al., 2016).

In this context, 2D perovskites offer a unique and tuneable crystal and electronic structure to exploit new physical, electronic, and optical properties. From the structural point of view, the 2D perovskites are

[1]Universidade da Coruña, Quimolmat, Centro de Investigacións Científicas Avanzadas (CICA), Rúa As Carballeiras, 15071 A Coruña, Spain

[2]Department of Chemistry, Division of Applied Physical Chemistry, KTH Royal Institute of Technology, SE 100 44 Stockholm, Sweden

[3]CELLS-ALBA Synchrotron Light Facility, Cerdanyola del Vallès, 08290 Barcelona, Spain

[4]Lead contact

*Correspondence: alberto.garcia.fernandez@udc.es (A.G.-F.), m.andujar@udc.es (M.S.-A.)

https://doi.org/10.1016/j.isci.2022.104450

composed of alternating organic cations and inorganic sheets of PbX_6 octahedra. This peculiar structural arrangement confers a singular electronic scenario with large differences in the dielectric permittivity between the organic (low dielectric permittivity) and inorganic layers (large dielectric permittivity) (Srimath Kandada and Silva, 2020). This gives rise to a fascinating multiple-pseudo quantum-well structure in which the inorganic layers serve as the potential wells and the organic layers as the potential barriers. This unique property makes these 2D perovskites a strong candidate for light emission applications (Krishna et al., 2018).

In addition, 2D perovskites have shown great potential as semiconductor ferroelectrics (FE) (Wu et al., 2018; Liao et al., 2015). Furthermore, the semiconductive FE materials can be exploited as polarization-sensitive photodetectors (Li et al., 2019) and for the conversion of light energy into photovoltaic devices, where the electron-hole pair is selectively separated toward the electrodes by the electric field of the polarization. This latter eludes the use of selective application layers and simplifies the manufacturing of the solar cell devices.

An interesting aspect of oxidic 2D perovskites, which is still poorly studied on 2D hybrid layered perovskites, is their thermomechanical response. It is well-known and understood that most materials exhibit positive thermal expansion (PTE) upon heating because of the increase in the amplitude of atomic bond vibrations with temperature. This phenomenon usually occurs along all three crystallographic axes, with typical values of linear thermal expansion, α, in the range $1MK^{-1} < \alpha < 20\ MK^{-1}$. In very rare cases, structural, magnetic, or electronic peculiarities may give rise either to anomalous thermomechanical responses among them: a) negative thermal expansion (NTE), when lattice dimensions shrink upon heating, b) colossal thermal expansion, in which the coefficient of linear thermal expansion has a magnitude, $|\alpha| > 100\ MK^{-1}$, c) near-zero thermal expansion (ZTE), when TE coefficients keep close to zero over a large temperature range, and d) anisotropic thermal expansion, when there is a coexistence of PTE, NTE, or ZTE along the three crystallographic axes within a single material. Thermal expansion is a typical example of the influence of external stimuli on the properties of a material and can easily be rationalized as responses that occur at the atomic level, although the exact mechanisms may not always be obvious (Das et al., 2010). Colossal PTE, NTE, and ZTE materials have many applications, such as dental fillings, cooker hobs, or high-precision optics, and are highly desirable for the future design of sensitive thermomechanical actuators.

In this work, we have revisited the layered hybrid perovskites of general formula A_2PbCl_4 and A_2PbBr_4 (Figure 1) with A cyclohexylammonium ($C_6H_{11}NH_3^+$ or CHA) or cyclopentylammonium ($C_5H_9NH_3^+$ or CPA). We are interested in such materials because the presence of nonaromatic rings in the organic A slabs with a larger degree of freedom could in principle promote interesting phase transitions close to room temperature and also anomalous thermomechanical responses.

These compounds had been synthesized and their crystal structures had been elucidated by Billing and Lemmerer in 2009 (Billing and Lemmerer, 2009) at T = 173K. From the structural point of view, all these compounds are composed by inorganic layers of corner-sharing PbX_6 octahedra and organic cations between

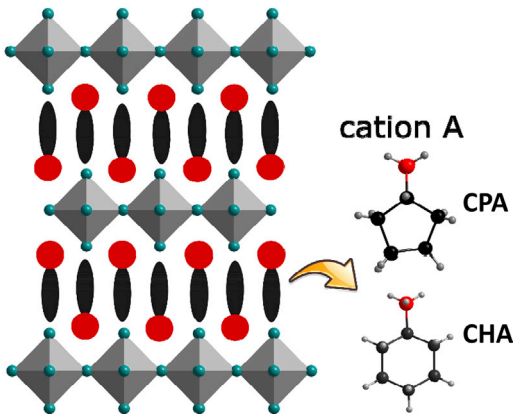

Figure 1. Schematic draw of the crystal structure of the A_2PbX_4 compounds, where A can be cyclohexylammonium ($C_6H_{11}NH_3^+$ or CHA) or cyclopentylammonium ($C_5H_9NH_3^+$ or CPA) and X can be Cl^- or Br^- anions

Colors code: N (red spheres), C (black spheres), H (gray spheres), Cl^-/Br^- (green spheres).

the inorganic layers. The ammonium group of the organic cations is in all cases located in the cavities defined by four corner-of PbX_6 sharing octahedral (see Figure 1).

Out of these four compounds, $(CHA)_2PbBr_4$ is already known to show outstanding properties at room temperature, such as photoferroelectric response, with an exceptional anisotropic bulk photovoltaic effect (Sun et al., 2016), ferroelectric behavior (Ye et al., 2016) and white-light emission in thin film. (Yangui et al., 2015a). Meanwhile, the other three compounds have not been studied beyond their previous structural characterization at low temperature (Billing and Lemmerer, 2009), up to our knowledge.

In this work, we have studied the thermal evolution of their crystal structure above room temperature using DSC analysis and synchrotron powder X-ray diffraction. In addition, we have explored their thermomechanical response above room temperature. Moreover, we have also studied their functional properties, such as UV-vis light absorbance, photoluminescence spectra, and dielectric properties.

RESULTS AND DISCUSSION

Synthesis and basic characterization

To check the purity of the obtained samples, they were studied by powder X-ray diffraction. Comparison of their experimental PXRD patterns with the profile obtained from their single crystal structure (Billing and Lemmerer, 2009) (Figure S1) confirmed that they are single phase materials. It is worth to note that the experimental pattern of $(CPA)_2PbCl_4$ is strongly influenced by preferred orientation, which causes excessive intensity in the peaks along [100] direction.

Besides, the thermal stability of the obtained materials was determined by TGA analysis. According to the results shown in Figure S2, the $(CHA)_2PbX_4$ and $(CPA)_2PbCl_4$ compounds are stable up to T$\sim$ 500K. At higher temperatures, they decompose in two steps: a first weight loss ($\sim$50%) at T$\sim$ 500–650 K, which corresponds to the release of two organic cations and two halide anions and a second weight loss ($\sim$50%) at T$\sim$ 700–950 K, which corresponds to the volatilization of the remaining lead halide.

Differential scanning calorimetric (DSC) analyses

DSC experiments reveal that these compounds undergo several reversible phase transitions above room temperature (see Figure 2). The changes in enthalpy ΔH and the entropy ΔS of these phase transitions were determined from the area of the heat flow peaks, whose values are shown in Table S1. The values of ΔH of these compounds are similar to those reported in the literature for related layered hybrid perovskites (Billing and Lemmerer, 2007). Here, the number of configurations in a disordered system, N, can be estimated by using the relation $\Delta S = R \ln(N)$, where R is the gas constant. Therefore, assuming an order-disorder transition, we obtain values ranging between one and 3 (see Table S1), which are similar to those reported from other related compounds (Wang et al., 2015).

Variable temperature synchrotron powder X-Ray diffraction (SPXRD)

To adequately characterize the multiple crystalline phases and their phase transitions, we have collected variable temperature synchrotron powder X-ray diffraction (SPXRD) patterns. The obtained patterns were analyzed using a LeBail refinement, which allows us to obtain information about the different polymorphs presented by these compounds as a function of temperature and determine the linear thermal expansion coefficients of the different crystalline structures. For the space group assignment of the unknown phases, to begin with, we refined the highest temperature phases with the aristotype space group *I4/mmm (nº 139)* of the A_2BX_4 Ruddlesden-Popper structure (McNulty and Lightfoot, 2021). This space group was adequate for the refinement of SPXRD patterns of the $(CHA)_2PbBr_4$ and $(CPA)_2PbCl_4$ compounds, but it was unsatisfactory for the $(CPA)_2PbBr_4$ compound (see discussion below). The lower temperature patterns were refined using space groups of lower symmetry than that of the parent phase, following a group-subgroup or supergroup relationship and taking into account the crystal structures previously described in the literature.

It is worth noting that the LeBail refinement of the SPXRD patterns $(CPA)_2PbBr_4$ and $(CPA)_2PbCl_4$ reveal the presence of a very small amount of $PbBr_2$ or $PbCl_2$, respectively. But most probably, these impurities are induced by the high intensity of the synchrotron beam and are not present in the as-synthesized sample as the conventional PXRD patterns do not show any trace of $PbBr_2$ or $PbCl_2$.

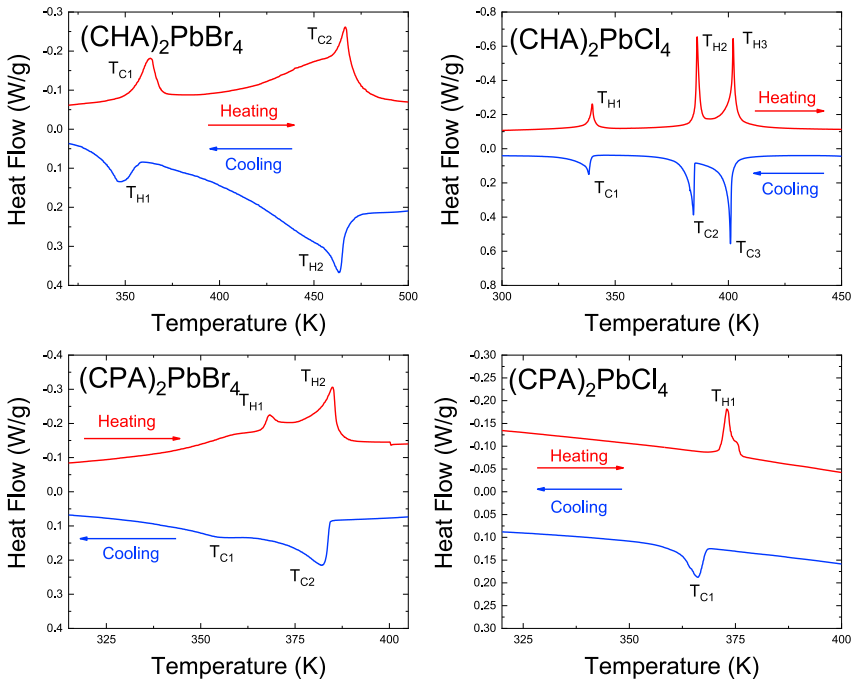

Figure 2. Differential scanning calorimetry curves for $(CHA)_2PbBr_4$, $(CPA)_2PbBr_4$, $(CHA)_2PbCl_4$ and $(CPA)_2PbCl_4$ compounds in cooling and heating cycles

$(CHA)_2PbBr_4$ compound

From the analysis of SPXRD patterns on the $(CHA)_2PbBr_4$ compound, two phase transitions were observed, which is in agreement with DSC results (see Figure S3). The small differences in the temperature of the phase transitions are because of the different heating rates in both techniques.

The lower temperature transition $T_{t1}\sim$ 350 K is related to a phase transition from the orthorhombic polymorph I (polar space group $Cmc2_1$) to the orthorhombic polymorph II (nonpolar space group *Cmca)* (Sun et al., 2016). Meanwhile, the higher temperature phase transition ($T_{t2}\sim$ 450 K) corresponds to the transformation of polymorph II into polymorph III, which shows a new tetragonal symmetry with space group *I4/mmm* (identified by LeBail refinement), see Figure S4. It is worth to note that the orthorhombic polymorphs I and II are superstructures of the tetragonal polymorph III, whose cell parameters are: $a_{ortho} \sim c_{tetra}$, $b_{ortho}\sim\sqrt{2}a_{tetra}$, $c_{ortho}\sim\sqrt{2}a_{tetra}$. It is worth noting that a_{ortho} and c_{tetra} parameters correspond to the layering axis and thus are related to the distance between adjacent inorganic layers separated by the organic cations. Meanwhile b_{ortho}, c_{ortho} and a_{tetra} are in-plane axis, which are then related to distances and angles in the inorganic layers (Pb-X bond length and Pb-X-Pb angles).

Figure 3 shows the thermal evolution of the lattice parameters of $(CHA)_2PbBr_4$, which have been obtained from LeBail fitting of the SXRPD patterns at different temperatures. As it can be seen there, a rather abrupt structural phase transition occurs at $T_t\sim$ 350 K, which is associated with a ferroelectric to paraelectric phase transition. Meanwhile, the high temperature phase transition from polymorph II to polymorph III is more gradual and almost isochoric.

$(CPA)_2PbBr_4$ compound

In the case of the $(CPA)_2PbBr_4$ compound, analysis of the SXRPD patterns shows two phase transitions (see Figure S5) in agreement with the DSC results. The lower temperature transition $T_{t1}\sim$ 350 K is related to a phase transition between the polymorph I (with monoclinic symmetry and space group $P2_1/c$) and polymorph II (with orthorhombic symmetry and space group *Cmca)*. Meanwhile, the higher temperature phase transition ($T_{t2}\sim$ 380 K) corresponds to the transformation of polymorph II into polymorph III, which shows a tetragonal symmetry with space group *P4/mmm* according to our LeBail refinement of the synchrotron patterns, see Figure S6.

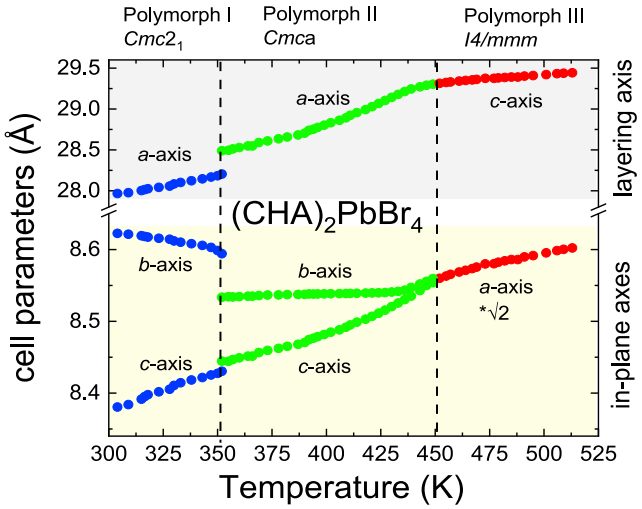

Figure 3. Temperature dependence of the cell parameters of polymorph I, II, and III for $(CHA)_2PbBr_4$ compound

It is worth to note that we have first tried to fit the highest temperature phase also to space group *I4/mmm*. Nevertheless, as some peaks could not be fitted (see inset of Figure S6), we reduced the symmetry and used instead space group *P4/mmm* (nº 123), which is a subgroup of the space group I4/mmm with loss of centering translation, thus achieving a good fit (see inset of Figure S6). That is the reason for the different assignment of space groups to the other compounds reported here.

Figure 4 shows the thermal evolution of the lattice parameters obtained from Le Bail fitting of the SPXRD patterns at different temperatures. As in the previous $(CHA)_2PbBr_4$ compound, the cell parameters (*b*-ortho and *c*-ortho) of $(CPA)_2PbBr_4$ exhibit a gradual merge, which results into a single one (*a*-tetra) when transforming into polymorph III. Therefore, the difference between the in-layering axes decreases at higher temperatures. This phenomenon occurs because the inorganic layers tend to regularize in the high symmetry tetragonal ideal structure as previously observed for $(CHA)_2PbI_4$ (Yangui et al., 2015b).

$(CPA)_2PbCl_4$ compound

From the analysis of SXRPD patterns of the $(CPA)_2PbCl_4$ sample, only one phase transition occurring at $T_t \sim$ 340 K (see Figure S7) is detected. According to our LeBail refinement (Figure S8), this transition

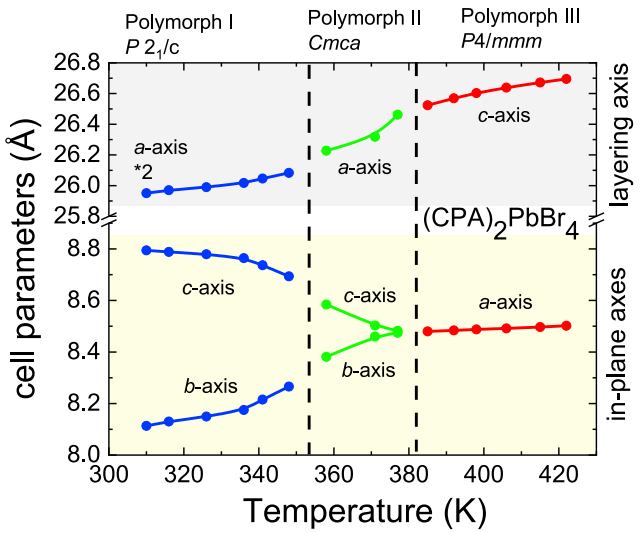

Figure 4. Temperature dependence of the cell parameters of polymorph I, II, and III for $(CPA)_2PbBr_4$ compound

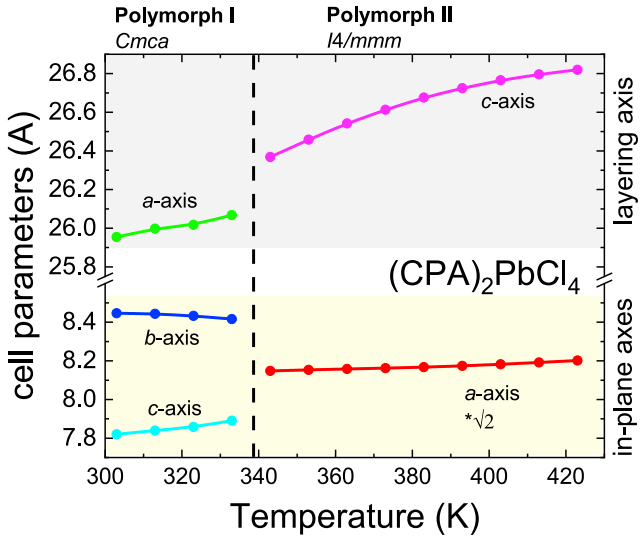

Figure 5. Temperature dependence of the cell parameters of polymorph I and II for $(CPA)_2PbCl_4$ compound

corresponds to the transformation of the lower temperature polymorph (orthorhombic symmetry and space group *Cmca*) into a higher temperature polymorph (tetragonal symmetry and space group *I4/mmm*).

Figure 5 shows the thermal evolution of the lattice parameters. Similar to the previous compounds, the in-plane *b-ortho* and *c-ortho* axes of $(CPA)_2PbBr_4$ exhibit a gradual merge, which is completed when transforming into polymorph II.

In summary, we have been able to expand the phase diagrams of the $(CHA)_2PbX_4$ and $(CPA)_2PbX_4$ ($X = Br^-$ and Cl^-) compounds by DSC analysis and variable temperature synchrotron powder X-ray diffraction. Figure 6 summarizes the crystal systems and space groups adopted by these four compounds. Therefore, the here studied compounds exhibit a very rich structural phase diagram with multiple phase transitions, which in fact enlarge the structural diversity of the emerging family of 2D- organic-inorganic perovskites compounds, A_2BX_4, with previous members $(CHA)_2CdBr_4$ (Yangui et al., 2018) and $(CHA)_2PbI_4$. (Yangui et al., 2015b).

Thermal expansion (TE) analysis

We have observed that the cell parameters of these compounds exhibit anomalous thermal evolutions. In this context we have calculated the linear (α) and volumetric (β_V) coefficients of the thermal expansion (TE) from the obtained cell parameter data by using the web-based tool PASCal (principal axis strain calculator; http://pascal.chem.ox.ac.uk). (Cliffe and Goodwin, 2012) The obtained results are shown in Figure 7 and

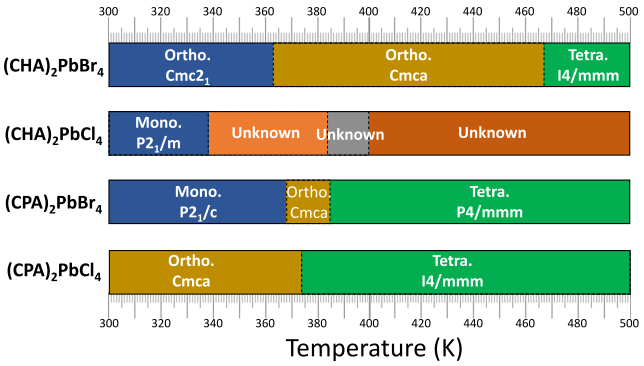

Figure 6. Phase diagram with crystal systems and space group for $(CHA)_2PbX_4$ and $(CPA)_2PbX_4$ ($X = Br^-$ and Cl^-) for $T \geq 300$ K

Table S2. Remarkably, these results reveal in first place the following interesting features for all the studied compounds:

(i) The highest temperature (tetragonal) polymorphs always exhibit positive TE (for α and β_V).

(ii) In all lower temperature polymorphs, α is highly anisotropic and exhibits both positive and negative values, whereas β_V is always positive,

(iii) In all studied compounds, most of α and β_V values are colossal ($\alpha > 100\ MK^{-1}$, $\beta_V = 10–40\ MK^{-1}$) and considerably higher than in other hybrid layered perovskites (Spanopoulos et al., 2019). For example, these compounds surpass the volumetric TE coefficients of analogous compounds, such as $(CHA)_2PbI_4$ (178 MK^{-1} between 295 and 360 K),(Yangui et al., 2015c), $(FA)SnI_3$ (174 MK^{-1} between 150 and 225 K), and $(FA)PbBr_3$ (219 MK^{-1} between 150 and 250 K), where FA is formamidinium (Schueller et al., 2018). In that regard, and very remarkably, our studies show that polymorph II of $(CHA)_2PbBr_4$ exhibits a new record volumetric TE coefficient of 480 MK^{-1}, which is more than two

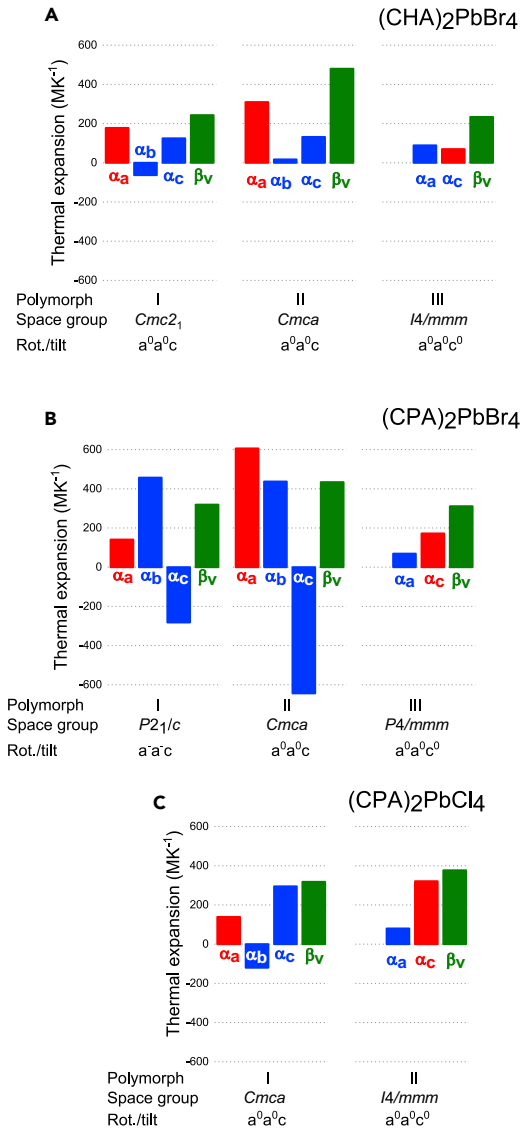

Figure 7. Linear TE coefficients, a, and the volumetric TE coefficient, b_V, for (a) $(CHA)_2PbBr_4$, (b) $(CPA)_2PbBr_4$, and (c) $(CPA)_2PbCl_4$. Colour code: red (linear TE coefficients along layering axis), blue (linear TE coefficients in-plane axes) and green (volumetric TE coefficient).

times the previous record held by (FA)$PbBr_3$, up to now the highest TE coefficient reported for any extended inorganic crystalline solid (Schueller et al., 2018).

More in detail, in all the compounds studied here, colossal positive thermal expansion occurs along the layering axis. We attribute this effect to the significant increase in the dynamic motion of the organic cations upon heating, which is difference with the case of purely inorganic 2D-perovskites (Ablitt et al., 2018).

On the other hand, the in-plane axes of low temperature polymorphs are seen to experience not only positive but very remarkably negative (NTE) as well as almost zero TE coefficients. This gives rise to the very rarely encountered situation (Phillips and Fortes, 2017) of having a material with colossal TE in one direction together with zero expansion in the perpendicular one. This is the case, for example, for polymorph II of $(CHA)_2PbBr_4$, which shows a colossal positive TE along the layering *a*-axis (α_a = 310 MK^{-1}) and almost zero TE along the perpendicular in-plane *b*-axis (α_b = 17 MK^{-1}) in the temperature range 350K < T < 450 K.

Trying to understand the origin of the peculiar thermal behavior of in-plane axes, we have looked at the few $A_{n+1}B_nO_{3n+1}$ Ruddlesden–Popper (RP)-layered perovskites that show uniaxial NTE (Ablitt et al., 2018),(Ablitt et al., 2017) Interestingly, in such oxidic compounds, NTE is seen to only occur along the layering axis and it is always associated with rotations of BO_6 octahedra about the layering axis, whereas no tilt about in-plane axes is present. In that regard, it should be indicated that in RP phases, because of their well-defined layering axis, it is customary to distinguish between rotations and tilts (see Figure S9) in that manner (Ablitt et al., 2020).

To see if rotation/tilts of PbX_6 in the inorganic slabs could also be playing a role in the compounds studied here, from the cell symmetry and space group of each polymorph we have estimated the possibility of such distortions following the work of J. A. McNulty and Philip Lightfoot and using the extended Glazer-like notation (McNulty and Lightfoot, 2021).

As indicated in detail in Table S3 and more schematically in Figure 7, in our compounds, the different polymorphs display one of following three different rotation-tilt systems, namely:

i) $a^0a^0c^0$ ideal configuration without rotation or tilting;

ii) a^0a^0c with rotation about the layering axis and without tiltings about in plane axes;

iii) a^-a^-c with both rotations about the layering direction and in plane tiltings

Besides, it is important to note that high temperature polymorphs are the ones to show the presence of conventional PTE with neither octahedral rotation nor tilting. Meanwhile those polymorphs with anomalous negative or almost zero TE exhibit in all cases rotations about the layering axis. Therefore, rotations of PbX_6 seem to be playing an important role in the thermomechanical responses reported here.

Moreover, we have identified that such rotations in the low temperature polymorphs go together with a distortion of the equatorial plane of the octahedra in the inorganic slab. For example, the *Cmca* phases display two different Pb-X bond lengths and two different X-Pb-X bond angles, in which one is lower and one is higher than the ideal 90°(Billing and Lemmerer, 2009) (Ye et al., 2016). This is caused by the location of the X^- anion in the special crystallographic site (0, y, z), with 2° of freedom within the layering plane, thus resulting in a "wine-rack" effect which accounts for the observed in-plane anomalous thermomechanical response. As depicted in Figure 8, the cooperative rotation together with the octahedral distortion can cause expansion in one direction coupled with a zero expansion or an NTE in a perpendicular direction.

Thus in the low temperature phases, which noticeably exhibit more degrees of freedom than the high temperature phases, the thermal evolution of the position of the X^- anion along the *in-plane* axes is also a key parameter for their thermomechanical response, which is anisotropic and can be positive, negative, or zero depending on how these evolve upon heating or cooling; see a schematic summary of all the here reported TE behaviors in Figure S10.

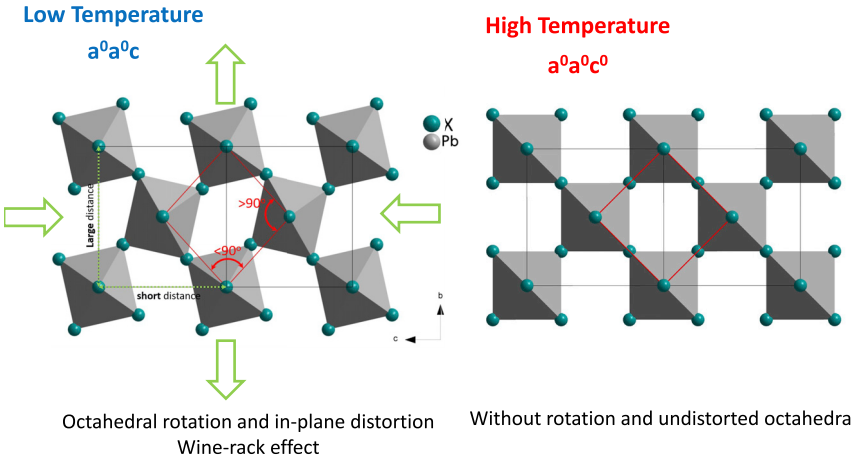

Figure 8. Scheme showing the octahedral arrangement viewed along the layering axis for the high temperature phases with $a^0a^0c^0$ rotation/tilts system (right figure) and low temperature phases with a^0a^0c rotation/tilt system (left figure)

Dielectric properties

Relative permittivity versus temperature measurements allowed us to better understand the mechanism of the observed phase transitions of these compounds. It is worth mentioning that the dielectric properties of $(CHA)_2PbCl_4$, $(CPA)_2PbBr_4$ and $(CPA)_2PbCl_4$ compounds are studied here for the first time.

Figure 9 shows the temperature dependence of the real part of the complex dielectric permittivity (the so-called relative dielectric permittivity, ε_r'). Very interestingly, all these compounds exhibit an anomaly and/or sharp increase of ε_r' occurring at a temperature close to the phase transitions observed by DSC. All three compounds exhibit a common trend, as follows: (i) at room temperature, the ε_r' values are relatively low (around 20) and almost frequency independent; and (ii) in the vicinity of the phase transition temperatures, the ε_r' values largely increase upon heating and display large frequency dependence.

About the origin of the observed dielectric transition, in the case of the $(CHA)_2PbBr_4$ compound, it has been reported that it is because of a ferroelectric to paraelectric transition from a non-centrosymmetric to a centrosymmetric space group (Ye et al., 2016). In the case of the other compounds, all obtained crystal structures are centrosymmetric, and therefore, they exhibit a different mechanism.

In this context, it is important to note the similarity between the dielectric transitions displayed by the here presented compounds and those observed in the related hybrid organic-inorganic compounds, such as $(DMA)PbX_3$ (García-Fernández et al., 2019), $(MA)PbX_3$ (Onoda-Yamamuro et al., 1992), and $(DMA)_7Pb_4X_{15}$ (García-Fernández et al., 2018) (where X = Cl^-, Br^- and I^-, DMA = dimethylammonium cation, MA = methylammonium cation), whose origin has been related to order-disorder processes of the polar DMA^+ and MA^+ cations. In all these systems (and other related compounds) (Liao et al., 2015; Shi et al., 2019; Mączka et al., 2019), the high temperature phase shows reorientations of the electrical dipoles associated with the organic cations with respect to the inorganic framework. Meanwhile, in the low temperature phase, the cations and their associated dipoles get ordered and are basically frozen.

In the systems studied here, we suggest a similar mechanism. In the $(CHA)_2PbBr_4$, $(CPA)_2PbBr_4$ and $(CPA)_2PbCl_4$ compounds, order-disorder processes would be responsible for the sharp increase of the ε_r' values in the vicinity of the phase transitions. In the aforementioned compounds, both $(CHA)^+$ and $(CPA)^+$ cations are polar species, where the dipole moments display an antiparallel arrangement in the room temperature phases. However, these cations are dynamically disordered above room temperature, which highly increases the ε_r' values.

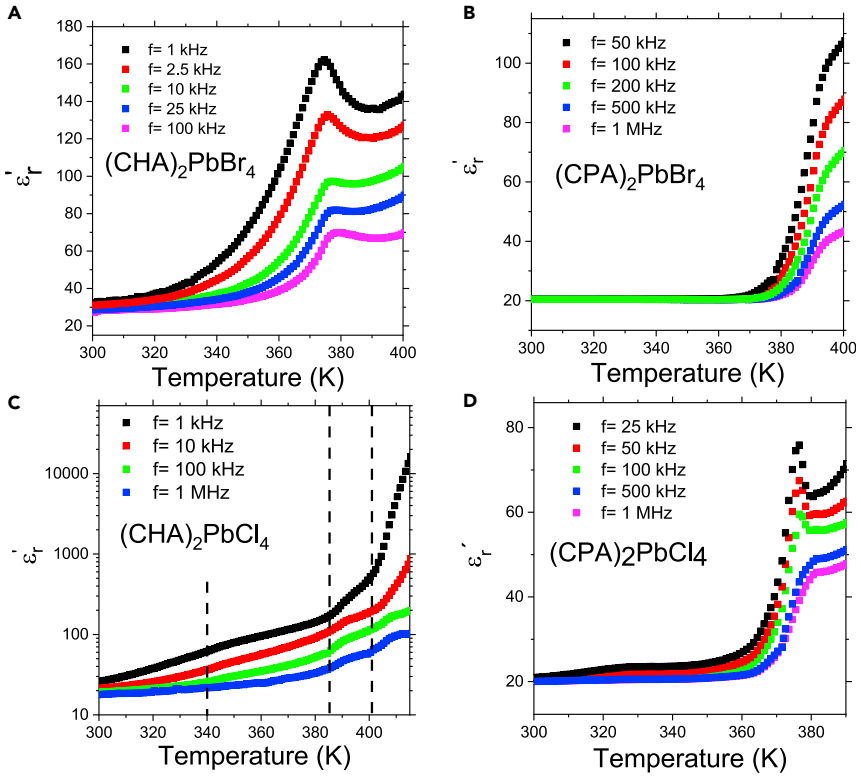

Figure 9. Temperature dependence of the real part of the complex dielectric permittivity for (a) $(CHA)_2PbBr_4$, (b) $(CPA)_2PbBr_4$, (c) $(CHA)_2PbCl_4$ and (d) $(CPA)_2PbCl_4$.

In view of the obtained large values of the dielectric permittivity and to make sure that they are really intrinsic, we have analyzed the loss tangent vs temperature curves; see Figure S11. The obtained data indicate that the loss tangent values markedly increase for temperatures higher than 380 K, in particular for the $(CHA)_2PbCl_4$ compound. These results indicate that the obtained large values of the dielectric permittivity are enhanced by the presence of extrinsic contributions such as space charges at the interface between electrode-sample.

UV-visible spectroscopy

We studied the photo-response of the obtained materials by UV-vis absorption at room temperature and by photoluminescence (PL) at different temperatures. Figure 10 shows the absorbance spectra of these compounds at room temperature; all of them display a sharp absorption edge around the UV spectral region.

The absorbance spectra show a wavelength cut-off of ~ 350 nm and ~ 425 nm for the Cl^- Br^- compounds, respectively. In turn, the corresponding optical band gaps (E_g), determined using the Kubelka–Munk equation, range from 2.90 to 3.51 eV, see Table 1 and Figure S12. In agreement with the literature results, our compounds show a bathochromic shift with the halide anion, from Cl^- to Br^-. In addition, the bandgaps estimated here are comparable to other analogous compounds with general formula $(R\text{-}NH_3)_2PbX_4$ layered perovskite halides (Zhang et al., 2011).

Moreover, the solid steady-state photoluminescence (PL) spectra were measured at different temperatures. According to the obtained results, all A_2PbX_4 compounds do not exhibit detectable PL emission at room temperature. Therefore, the PL emission is quenched at room temperature because of nonradioactive recombination, such as lattice or molecular vibrations. Nevertheless, as shown in Figure 11, at T = 100 K these compounds exhibit a broad PL emission with peak maxima and full width half-maximum (FWHM) summarized in Table 1. The corresponding CIE chromaticity coordinates are reported at Figure S13;

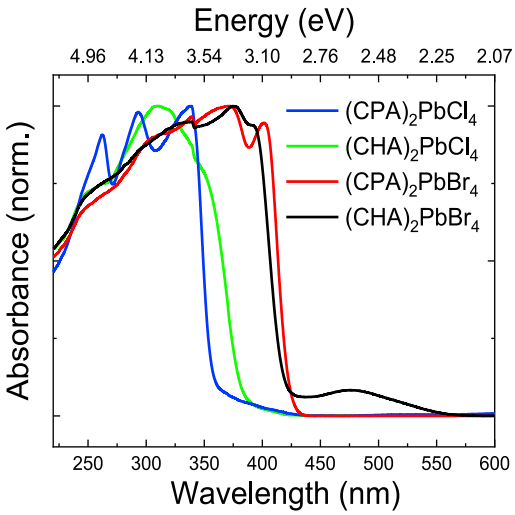

Figure 10. UV-vis absorbance spectra at room temperature

besides, in these compounds, the PL emission occurs between blue and yellow color of the visible region of the spectra.

It is worth noting that the $(CPA)_2PbBr_4$ compound exhibits a different PL emission from that shown by the other compounds. In fact, $(CPA)_2PbBr_4$ exhibits two PL emission peaks: one intense and sharp peak with a maximum around 406 nm and a second peak less intense with a maximum around 510 nm. This second PL emission peak shows similar characteristics to these observed by the other compounds.

In addition, we have recorded the photoluminescence excitation (PLE) spectra of these compounds (Figure 12), and the maxima absorption (λ_{ab}) and emission (λ_{em}) wavelengths exhibit a remarkably large shift, indicating very large Stokes shifts, see Figure 12.

Furthermore, the $(CPA)_2PbBr_4$ compound exhibits a singular response. This material shows an intense and sharp PL peak at $\lambda_{em}\sim$ 406 nm, which overlaps with the absorption peak observed in the PLE and absorbance spectra. Therefore, no Stokes-shift is observed there. Taking similar observations in the literature into account (Dohner et al., 2014), we suggest that the PL emission exhibits the typical characteristics of free-exciton recombination: narrow emission and minimal Stokes-shift.

In contrast with this sharp peak, the remaining low-energy and broad emission peaks observed in these four compounds suggest the typical PL emission of self-trapped excitons (STEs) (Smith et al., 2019).

In this case, the PL emission is commonly influenced by the structural distortion of inorganic frameworks (Mao et al., 2017), which can be tuned by the nature of the A cations and the X anions, as well as by external applied pressure (Liu et al., 2018). In that regard, we have analyzed different structural

Table 1. Optical parameters obtained from the absorbance and PL spectra for A_2PbX_4 compounds: Optical bandgap (E_g), emission wavelength (λ_{em}) [in units of eV], and full width at half-maximum (FWHM)

Compound	E_g (eV)	λ_{em} (nm)/E_{em} [eV]	HWHM (eV)
$(CHA)_2PbBr_4$	2.96	560 [2.21]	0.46
$(CHA)_2PbCl_4$	3.33	545 [2.27]	0.54
$(CPA)_2PbBr_4$	2.90	510 [2.43] 406 [3.05]	0.62 0.08
$(CPA)_2PbCl_4$	3.51	435 [2.85]	0.58

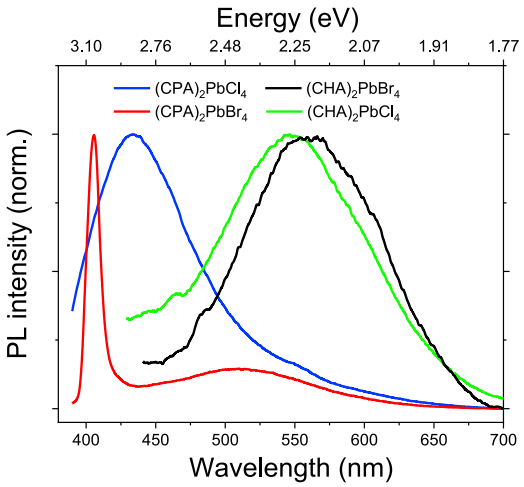

Figure 11. Normalized PL emission spectra at 100K

parameters to identify the most influential on the PL emission. Our analysis shows a linear relation between the octahedral distortion versus the Stokes-shifts (Figure 13), which was estimated as the difference E_g - E_{em}. Our data agree with those reported for analogous compounds such as $(CHA)_2CdBr_4$, which exhibits a broad white-light PL emission because of the structural distortion of the $CdBr_6$ octahedra (Yangui et al., 2018).

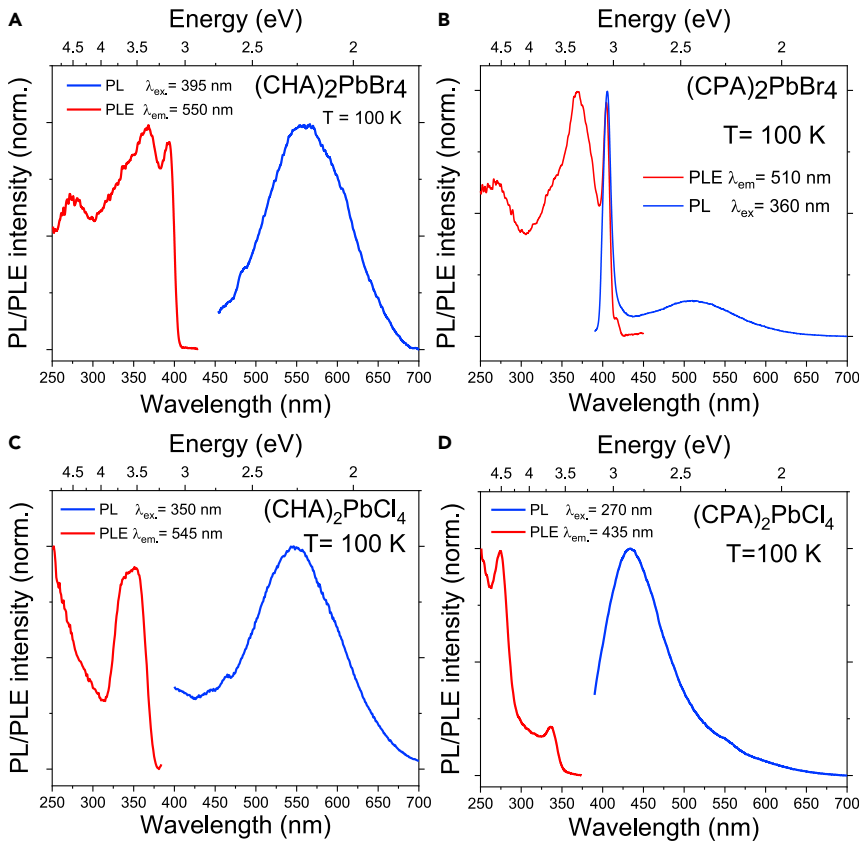

Figure 12. Normalized PLE and PL emission spectra for (a) $(CHA)_2PbBr_4$, (b) $(CPA)_2PbBr_4$, (c) $(CHA)_2PbCl_4$ and (d) $(CPA)_2PbCl_4$. compounds at T= 100K.

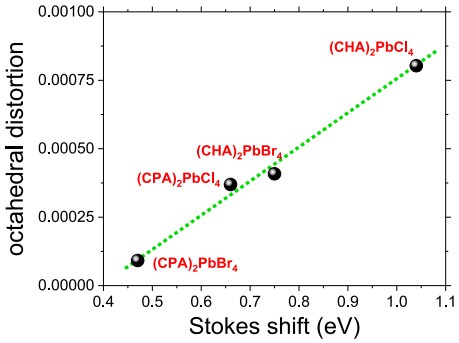

Figure 13. Representation of octahedral distortion versus Stokes-shift of A_2PbX_4 compounds

Comparing the influence of both organic cations, we have observed that CHA^+ provokes a higher structural distortion and Stokes-shift than CPA^+. Moreover, we also observe that the chloride compounds have a larger structural distortion and Stokes-shift than the bromide ones. Quite remarkably, the less distorted compound is $(CPA)_2PbBr_4$, which is also the only material in this work that exhibits a free-exciton recombination.

To quantify the octahedral distortion Δd, we have used the following expression based on the Pb-X bond lengths

$$\Delta d = \left(\frac{1}{6}\right)\sum_{n=1}^{6}\left[\frac{d_n - d}{d}\right]^2$$

where d is the mean Pb−X distance and d_n are the six individual Pb−X distances. (Alonso et al., 2000) The Pb-X bond lengths were obtained from crystal structures reported by Billing and Lemmerer (2009).

Conclusions

We have revisited the crystal structures and functional properties of the lead-halide-layered perovskites of general formula A_2PbX_4, where A is cyclohexylammonium (CHA^+) or cyclopentylammonium (CPA^+) cation and X is Cl^- or Br^- anion. These compounds exhibit several polymorphs above room temperature and interesting functional properties. Using differential scanning calorimetry, we have observed the following transitions: (i) in $(CHA)_2PbBr_4$ we find two transitions at around 367 and 466 K; (ii) $(CHA)_2PbCl_4$ shows three transitions at around 338, 385 and 402 K; (iii) in $(CPA)_2PbBr_4$ we observe two transitions at around 355 and 382 K; (iv) $(CPA)_2PbCl_4$ displays only one transition at around 372 K.

In addition, we have monitored the thermal evolution of their crystal structures using synchrotron X-ray powder diffraction. The obtained patterns confirm the phase transitions observed by DSC. Moreover, we have determined the cell parameters and space groups of their polymorphs for $T \geq 300K$, which allowed us to configure a more detailed phase diagram. Furthermore, the studies of dielectric permittivity also show thermally induced anomalies that confirm the observed phase transitions.

Very interestingly, these compounds also exhibit an outstanding thermomechanical response. For the lower temperature polymorphs, the evolution of the lineal TE is highly anisotropic, involving a uniaxial NTE and a colossal and almost zero TE in perpendicular directions. We attribute the origin of these peculiar behaviors to rotations about the layering axis and distortions of the PbX_6 octahedra in the inorganic layer, in the case of NTE, and to the increase of degrees of freedom in the organic layer in the case of colossal positive thermal expansion along the layering axis.

It is worth highlighting the record volumetric TE coefficient observed for the $(CHA)_2PbBr_4$ compound ($480\ MK^{-1}$), which is among the highest recorded for any extended inorganic crystalline solid. In addition, we predict that this anomalous TE can be present in other layered hybrid perovskites, and we encourage further exploration of the thermomechanical response of this interesting family of materials.

In addition, we have studied the absorption and emission UV-vis spectra of these materials at different temperatures. All these compounds exhibit a broad PL emission with large Stokes-shifts, which are related to an exciton PL emission. The PL emission is strongly influenced by the structural distortion of the inorganic framework. In particular, we have observed that the Stokes-shifts linearly increase with the distortion of the PbX_6 octahedra. We also expect that our findings will help to find optimized and controlled PL emissions by the design of new related structures with different degrees of distortion.

Limitations of the study

Le Bail refinement provides only limited structural information about the high temperature polymorphs. Further experiments will be necessary for a deeper knowledge on the crystal structure of the high temperature polymorphs.

STAR★METHODS

Detailed methods are provided in the online version of this paper and include the following:

- KEY RESOURCES TABLE
- RESOURCE AVAILABILITY
  - Lead contact
  - Materials availability
  - Data and code availability
- EXPERIMENTAL MODEL AND SUBJECT DETAILS
- METHOD DETAILS
  - General reagent information
  - Synthesis of A_2PbX_4 compounds
  - Powder X-Ray diffraction
  - Thermal analysis
  - Ultraviolet-visible (UV-Vis) spectroscopy
  - Dielectric properties
- QUANTIFICATION AND STATISTICAL ANALYSIS
- ADDITIONAL RESOURCES

SUPPLEMENTAL INFORMATION

Supplemental information can be found online at https://doi.org/10.1016/j.isci.2022.104450.

ACKNOWLEDGMENTS

This work was financially supported by the Ministerio de Ciencia e Innovación (MICINN) and EU-ERDF under the projects MAT2017-86453-R and PDC2021-121076-I00. We thank Alba synchrotron for the provision of beamtime at BL04-MSPD beamline (experiment 2019023280). We also thank prof. Dr. R. Artiaga and Dr. J.J. López-Beceiro (University of A Coruña) for assistance during DSC measurements. J.M.B.G. thanks Xunta de Galicia for a postdoctoral fellowship.

AUTHOR CONTRIBUTIONS

A.G-F., D.V-G., and M.S-A. envisioned, designed, and supervised the project. A.C-C., A.G-F., and D.V-G. prepared the samples and conducted the dielectric and PL experiments. C.P. conducted the synchrotron experiments. All authors contributed to the discussion of experimental results. The manuscript was written by all contributing authors.

DECLARATION OF INTERESTS

The authors declare no competing interests.

Received: December 23, 2021
Revised: May 2, 2022
Accepted: May 18, 2022
Published: June 17, 2022

REFERENCES

Ablitt, C., Craddock, S., Senn, M.S., Mostofi, A.A., and Bristowe, N.C. (2017). The origin of uniaxial negative thermal expansion in layered perovskites. npj Comput. Mater. *3*, 44–48. https://doi.org/10.1038/s41524-017-0040-0.

Ablitt, C., Mostofi, A.A., Bristowe, N.C., and Senn, M.S. (2018). Control of uniaxial negative thermal expansion in layered perovskites by tuning layer thickness. Front. Chem. *6*, 455. https://doi.org/10.3389/fchem.2018.00455.

Ablitt, C., McCay, H., Craddock, S., Cooper, L., Reynolds, E., Mostofi, A.A., Bristowe, N.C., Murray, C.A., and Senn, M.S. (2020). Tolerance factor control of uniaxial negative thermal expansion in a layered perovskite. Chem. Mater. *32*, 605–610. https://doi.org/10.1021/acs.chemmater.9b04512.

Alonso, J.A., Martínez-Lope, M.J., Casais, M.T., and Fernández-Díaz, M.T. (2000). Evolution of the Jahn−Teller distortion of MnO6 octahedra in RMnO3 perovskites (R = Pr, Nd, Dy, Tb, Ho, Er, Y): a neutron diffraction study. Inorg. Chem. *39*, 917–923. https://doi.org/10.1021/IC990921E.

Bandyopadhyay, B., Luitel, H., Sil, S., Dhar, J., Chakrabarti, M., Nath, P., Ray, P.P., and Sanyal, D. (2020). NMR study of defect-induced magnetism in methylammonium lead iodide perovskite. Phys. Rev. B *101*, 094417. https://doi.org/10.1103/PhysRevB.101.094417.

Bari, M., Bokov, A.A., and Ye, Z.G. (2020). Ferroelasticity, domain structures and phase symmetries in organic-inorganic hybrid perovskite methylammonium lead chloride. J. Mater. Chem. C *8*, 9625–9631. https://doi.org/10.1039/d0tc02124e.

Billing, D.G., and Lemmerer, A. (2007). Synthesis, characterization and phase transitions in the inorganic-organic layered perovskite-type hybrids [(Cn H2n + 1NH 3)2PbI4], n = 4, 5 and 6. Acta Crystallogr. B *63*, 735–747. https://doi.org/10.1107/S0108768107031758.

Billing, D.G., and Lemmerer, A. (2009). Inorganic–organic hybrid materials incorporating primary cyclic ammonium cations: the lead bromide and chloride series. CrystEngComm *11*, 1549. https://doi.org/10.1039/b819455f.

Chen, Q., De Marco, N., Yang, Y.M., Song, T.B., Chen, C.C., Zhao, H., Hong, Z., Zhou, H., and Yang, Y. (2015). Under the spotlight: the organic-inorganic hybrid halide perovskite for optoelectronic applications. Nano Today *10*, 355–396. https://doi.org/10.1016/j.nantod.2015.04.009.

Chen, X.-G., Song, X.-J., Zhang, Z.-X., Zhang, H.-Y., Pan, Q., Yao, J., You, Y.-M., and Xiong, R.-G. (2020). Confinement-driven ferroelectricity in a two-dimensional hybrid lead iodide perovskite. J. Am. Chem. Soc. *142*, 10212–10218. https://doi.org/10.1021/jacs.0c03710.

Cliffe, M.J., and Goodwin, A.L. (2012). PASCal : a principal axis strain calculator for thermal expansion and compressibility determination. J. Appl. Crystallogr. *45*, 1321–1329. https://doi.org/10.1107/S0021889812043026.

Das, D., Jacobs, T., and Barbour, L.J. (2010). Exceptionally large positive and negative anisotropic thermal expansion of an organic crystalline material. Nat. Mater. *9*, 36–39. https://doi.org/10.1038/nmat2583.

Dohner, E.R., Hoke, E.T., and Karunadasa, H.I. (2014). Self-assembly of broadband white-light emitters. J. Am. Chem. Soc. *136*, 1718–1721. https://doi.org/10.1021/ja411045r.

Dou, L., Yang, Y.M., You, J., Hong, Z., Chang, W.-H., Li, G., and Yang, Y. (2014). Solution-processed hybrid perovskite photodetectors with high detectivity. Nat. Commun. *5*, 5404. https://doi.org/10.1038/ncomms6404.

García-Fernández, A., Bermúdez-García, J.M., Castro-García, S., Llamas-Saiz, A.L., Artiaga, R., López-Beceiro, J.J., Sánchez-Andújar, M., and Señarís-Rodríguez, M.A. (2018). [(CH 3) 2 NH 2] 7 Pb 4 X 15 (X = Cl – and Br –), 2D-perovskite related hybrids with dielectric transitions and broadband photoluminiscent emission. Inorg. Chem. *57*, 3215–3222. https://doi.org/10.1021/acs.inorgchem.7b03217.

García-Fernández, A., Juarez-Perez, E.J., Bermúdez-García, J.M., Llamas-Saiz, A.L., Artiaga, R., López-Beceiro, J.J., Señarís-Rodríguez, M.A., Sánchez-Andújar, M., and Castro-García, S. (2019). Hybrid lead halide [(CH 3) 2 NH 2]PbX 3 (X = Cl − and Br −) hexagonal perovskites with multiple functional properties. J. Mater. Chem. C *7*, 10008–10018. https://doi.org/10.1039/C9TC03543E.

Kojima, A., Teshima, K., Shirai, Y., and Miyasaka, T. (2009). Organometal halide perovskites as visible-light sensitizers for photovoltaic cells. J. Am. Chem. Soc. *131*, 6050–6051. https://doi.org/10.1021/ja809598r.

Krishna, A., Gottis, S., Nazeeruddin, M.K., and Sauvage, F. (2018). Mixed dimensional 2D/3D hybrid perovskite absorbers: the future of perovskite solar cells? Adv. Funct. Mater. *29*, 1806482. https://doi.org/10.1002/adfm.201806482.

Larson, A.C., and Von Dreele, R.B. (2000). Generalized structure analysis system (GSAS). Los Alamos Natl. Lab. Rep. LAUR, 86–748.

Li, L., Liu, X., Li, Y., Xu, Z., Wu, Z., Han, S., Tao, K., Hong, M., Luo, J., and Sun, Z. (2019). Two-dimensional hybrid perovskite-type ferroelectric for highly polarization-sensitive shortwave photodetection. J. Am. Chem. Soc. *141*, 2623–2629. https://doi.org/10.1021/jacs.8b12948.

Liao, W.-Q., Zhang, Y., Hu, C.-L., Mao, J.-G., Ye, H.-Y., Li, P.-F., Huang, S.D., and Xiong, R.-G. (2015). A lead-halide perovskite molecular ferroelectric semiconductor. Nat. Commun. *6*, 7338. https://doi.org/10.1038/ncomms8338.

Liu, G., Gong, J., Kong, L., Schaller, R.D., Hu, Q., Liu, Z., Yan, S., Yang, W., Stoumpos, C.C., Kanatzidis, M.G., et al. (2018). Isothermal pressure-derived metastable states in 2D hybrid perovskites showing enduring bandgap narrowing. Proc. Natl. Acad. Sci. U S A. *115*, 8076–8081. https://doi.org/10.1073/pnas.1809167115.

Mączka, M., Ptak, M., Gągor, A., Stefańska, D., and Sieradzki, A. (2019). Layered lead iodide of [Methylhydrazinium] 2 PbI 4 with a reduced band gap: thermochromic luminescence and switchable dielectric properties triggered by structural phase transitions. Chem. Mater. *31*, 8563–8575. https://doi.org/10.1021/acs.chemmater.9b03775.

Mao, L., Stoumpos, C.C., and Kanatzidis, M.G. (2019). Two-dimensional hybrid halide perovskites: principles and promises. J. Am. Chem. Soc. *141*, 1171–1190. https://doi.org/10.1021/jacs.8b10851.

Mao, L., Wu, Y., Stoumpos, C.C., Traore, B., Katan, C., Even, J., Wasielewski, M.R., and Kanatzidis, M.G. (2017). Tunable white-light emission in single-cation-templated three-layered 2D perovskites $(CH_3CH_2NH_3)_4Pb_3Br_{10-x}Cl_x$. J. Am. Chem. Soc. *139*, 11956–11963. https://doi.org/10.1021/jacs.7b06143.

McNulty, J.A., and Lightfoot, P. (2021). Structural chemistry of layered lead halide perovskites containing single octahedral layers. IUCrJ *8*, 485–513. https://doi.org/10.1107/s2052252521005418.

Mitzi, D.B. (2007). Synthesis, Structure, and Properties of Organic-Inorganic Perovskites and Related Materials (Wiley-Blackwell), pp. 1–121. https://doi.org/10.1002/9780470166499.ch1.

Onoda-Yamamuro, N., Matsuo, T., and Suga, H. (1992). Dielectric study of CH3NH3PbX3 (X = Cl, Br, I). J. Phys. Chem. Solids *53*, 935–939. https://doi.org/10.1016/0022-3697(92)90121-S.

Pandey, R., Vats, G., Yun, J., Bowen, C.R., Ho-Baillie, A.W.Y., Seidel, J., Butler, K.T., and Seok, S.I. (2019). Mutual insight on ferroelectrics and hybrid halide perovskites: a platform for future multifunctional energy conversion. Adv. Mater. *31*, 1807376–1807426. https://doi.org/10.1002/adma.201807376.

Papavassiliou, G.C., and Koutselas, I.B. (1995). Structural, optical and related properties of some natural three- and lower-dimensional semiconductor systems. Synth. Met. *71*, 1713–1714. https://doi.org/10.1016/0379-6779(94)03017-Z.

Pedesseau, L., Sapori, D., Traore, B., Robles, R., Fang, H.-H., Loi, M.A., Tsai, H., Nie, W., Blancon, J.-C., Neukirch, A., et al. (2016). Advances and promises of layered halide hybrid perovskite semiconductors. ACS Nano *10*, 9776–9786. https://doi.org/10.1021/acsnano.6b05944.

Phillips, A.E., and Fortes, A.D. (2017). Crossover between Tilt Families and Zero Area Thermal Expansion in Hybrid Prussian Blue Analogues. Angewandte Chemie International Edition *56* (50), 15950–15953. https://doi.org/10.1002/anie.201708514.

Schueller, E.C., Laurita, G., Fabini, D.H., Stoumpos, C.C., Kanatzidis, M.G., and Seshadri, R. (2018). Crystal structure evolution and notable thermal expansion in hybrid perovskites formamidinium tin iodide and formamidinium lead bromide. Inorg. Chem. *57*, 695–701. https://doi.org/10.1021/acs.inorgchem.7b02576.

Senocrate, A., and Maier, J. (2019). Solid-state ionics of hybrid halide perovskites. J. Am. Chem.

Soc. *141*, 8382–8396. https://doi.org/10.1021/jacs.8b13594.

Shi, C., Han, X.B., and Zhang, W. (2019). Structural phase transition-associated dielectric transition and ferroelectricity in coordination compounds. Coord. Chem. Rev. *378*, 561–576. https://doi.org/10.1016/j.ccr.2017.09.020.

Smith, M.D., Connor, B.A., and Karunadasa, H.I. (2019). Tuning the luminescence of layered halide perovskites. Chem. Rev. *119*, 3104–3139. https://doi.org/10.1021/acs.chemrev.8b00477.

Spanopoulos, I., Hadar, I., Ke, W., Tu, Q., Chen, M., Tsai, H., He, Y., Shekhawat, G., Dravid, V.P., Wasielewski, M.R., et al. (2019). Uniaxial expansion of the 2D Ruddlesden–popper perovskite family for improved environmental stability. J. Am. Chem. Soc. *141*, 5518–5534. https://doi.org/10.1021/jacs.9b01327.

Srimath Kandada, A.R., and Silva, C. (2020). Exciton polarons in two-dimensional hybrid Metal-halide perovskites. J. Phys. Chem. Lett. *11*, 3173–3184. https://doi.org/10.1021/acs.jpclett.9b02342.

Sun, Z., Liu, X., Khan, T., Ji, C., Asghar, M.A., Zhao, S., Li, L., Hong, M., and Luo, J. (2016). A photoferroelectric perovskite-type organometallic halide with exceptional anisotropy of bulk photovoltaic effects. Angew. Chem. Int. Ed. Engl. *55*, 6545–6550. https://doi.org/10.1002/anie.201601933.

Tan, Z.-K., Moghaddam, R.S., Lai, M.L., Docampo, P., Higler, R., Deschler, F., Price, M., Sadhanala, A., Pazos, L.M., Credgington, D., et al. (2014). Bright light-emitting diodes based on organometal halide perovskite. Nat. Nanotechnol. *9*, 687–692. https://doi.org/10.1038/nnano.2014.149.

Toby, B.H. (2001). *EXPGUI* , a graphical user interface for *GSAS*. J. Appl. Crystallogr. *34*, 210–213. https://doi.org/10.1107/S0021889801002242.

Tsai, H., Nie, W., Blancon, J.-C., Stoumpos, C.C., Asadpour, R., Harutyunyan, B., Neukirch, A.J., Verduzco, R., Crochet, J.J., Tretiak, S., et al. (2016). High-efficiency two-dimensional Ruddlesden–Popper perovskite solar cells. Nature *536*, 312–316. https://doi.org/10.1038/nature18306.

Wang, Z.X., Liao, W.Q., Ye, H.Y., and Zhang, Y. (2015). Sequential structural transitions with distinct dielectric responses in a layered perovskite organic-inorganic hybrid material: [C4H9N]2[PbBr4]. Dalt. Trans. *44*, 20406–20412. https://doi.org/10.1039/c5dt03277f.

Wu, Z., Ji, C., Li, L., Kong, J., Sun, Z., Zhao, S., Wang, S., Hong, M., and Luo, J. (2018). Alloying *n* -Butylamine into $CsPbBr_3$ to give a two-dimensional Bilayered perovskite ferroelectric. Material. Angew. Chem. Int. Ed. Engl. *57*, 8140–8143. https://doi.org/10.1002/anie.201803716.

Yangui, A., Garrot, D., Lauret, J.S., Lusson, A., Bouchez, G., Deleporte, E., Pillet, S., Bendeif, E.E., Castro, M., Triki, S., et al. (2015a). Optical investigation of broadband white-light emission in self-assembled organic-inorganic perovskite (C6H11NH3)2PbBr4. J. Phys. Chem. C *119*, 23638–23647. https://doi.org/10.1021/acs.jpcc.5b06211.

Yangui, A., Pillet, S., Mlayah, A., Lusson, A., Bouchez, G., Triki, S., Abid, Y., and Boukheddaden, K. (2015b). Structural phase transition causing anomalous photoluminescence behavior in perovskite (C 6 H 11 NH 3) 2 [PbI 4]. J. Chem. Phys. *143*, 224201. https://doi.org/10.1063/1.4936776.

Yangui, A., Pillet, S., Garrot, D., Triki, S., Abid, Y., and Boukheddaden, K. (2015c). Evidence and detailed study of a second-order phase transition in the (C 6 H 11 NH 3) 2 [PbI 4] organic-inorganic hybrid material. J. Appl. Phys. *117*, 115503. https://doi.org/10.1063/1.4915509.

Yangui, A., Pillet, S., Bendeif, E.-E., Lusson, A., Triki, S., Abid, Y., and Boukheddaden, K. (2018). Broadband emission in a new two-dimensional Cd-based hybrid perovskite. ACS Photonics *5*, 1599–1611. https://doi.org/10.1021/acsphotonics.8b00052.

Ye, H.-Y., Liao, W.-Q., Hu, C.-L., Zhang, Y., You, Y.-M., Mao, J.-G., Li, P.-F., and Xiong, R.-G. (2016). Bandgap engineering of lead-halide perovskite-type ferroelectrics. Adv. Mater. *28*, 2579–2586. https://doi.org/10.1002/adma.201505224.

Zhang, F., Lu, H., Tong, J., Berry, J.J., Beard, M.C., and Zhu, K. (2020). Advances in two-dimensional organic–inorganic hybrid perovskites. Energy Environ. Sci. *13*, 1154–1186. https://doi.org/10.1039/c9ee03757h.

Zhang, S., Audebert, P., Wei, Y., Lauret, J.S., Galmiche, L., and Deleporte, E. (2011). Synthesis and optical properties of novel organic-inorganic hybrid UV (R-NH3)2PbCl4 semiconductors. J. Mater. Chem. *21*, 466–474. https://doi.org/10.1039/c0jm02121k.

Zhu, X.-H., Mercier, N., Riou, A., Blanchard, P., and Frère, P. (2002). (C4H3SCH2NH3)2(CH3NH3)Pb2I7: non-centrosymmetrical crystal structure of a bilayer hybrid perovskite. Chem. Commun. *2*, 2160–2161. https://doi.org/10.1039/B205543K.

STAR★METHODS

KEY RESOURCES TABLE

REAGENT or RESOURCE	SOURCE	IDENTIFIER
Chemicals, peptides, and recombinant proteins		
$PbBr_2$ (≥98%)	Sigma-Aldrich	CAS: 10031-22-8
$PbCl_2$ (98%)	Sigma-Aldrich	CAS: 7758-95-4
Cyclohexylamine ($C_6H_{11}NH_2$, ≥99.9%)	Sigma-Aldrich	CAS: 108-91-8
Cyclopentylamine ($C_5H_9NH_2$, ≥99%)	Sigma-Aldrich	CAS: 1003-03-8
HBr solution (≥47 wt. % in H_2O)	Sigma-Aldrich	CAS: 10,035-10-6
HCl solution (37 wt% in H_2O)	Sigma-Aldrich	CAS: 7647-01-0
Software and algorithms		
GSAS and EXPGUI software	A.C. Larson and R.B. Von Dreele, "General Structure Analysis System (GSAS)", Los Alamos National Laboratory Report LAUR 86–748 (2000). B. H. Toby, EXPGUI, a graphical user interface for GSAS, J. Appl. Cryst. 34, 210–213 (2001)	https://subversion.xray.aps.anl.gov/trac/EXPGUI
Mercury 2020.3.0	Cambridge Crystallographic Data Center (CCDC).	https://www.ccdc.cam.ac.uk/solutions/csd-core/components/mercury/
ColorCalculator 7.77	OSRAM Sylvania, Inc	https://www.osram.us/cb/tools-and-resources/applications/led-colorcalculator/index.jsp
web-based tool PASCal	M.J. Cliffe and A.L. Goodwin, J. Appl. Cryst. (2012). 45, 1321–1329.	http://pascal.chem.ox.ac.uk
OriginPro 2018	Origin Lab Corporation	https://www.originlab.com/
Other		
Siemens D-5000 diffractometer	Siemens	https://www.sai.udc.es/es/unidades/UAE/equipamiento
Synchrotron powder X-ray diffraction (BL04-MSPD beamline)	ALBA Synchrotron	https://www.cells.es/en/beamlines/bl04-mspd
Thermal Analysis SDT2960 equipment	Thermal Analysis	https://www.sai.udc.es/es/unidades/UEM/equipamiento
TA Instruments MDSC Q-2000	Thermal Analysis	https://www.tainstruments.com/dsc-q20aq2000-pack/
Jasco V-650 UV-Visible double-beam spectrophotometer	Jasco	https://jascoinc.com/products/spectroscopy/uv-visible-nir-spectrophotometers/
Horiba FluoroMax Plus-P spectrofluorometer	Horiba	https://www.horiba.com/int/products/detail/action/show/Product/fluoromax-1576/
Linkam THMS-LNP95 cooling system	Linkam	https://www.linkam.co.uk/t96
Solartron1260A Impedance/Gain-Phase Analyzer	Solartron Analytical's	https://www.ameteksi.com/products/frequency-response-analyzers/1260a-impedance-gain-phase-analyzer

RESOURCE AVAILABILITY

Lead contact

Further information and requests for resource and reagents should be directed to and will be fulfilled the by lead contact, Manuel Sánchez-Andújar (m.andujar@udc.es).

Materials availability

This study did not generate new unique reagents.

Data and code availability

Data reported in this paper will be shared by the lead contact upon request.

This paper does not report original code.

Any additional information required to reanalyze the data reported in this paper is available from the lead contact upon request.

EXPERIMENTAL MODEL AND SUBJECT DETAILS

The study does not use experimental models typical in the life sciences.

METHOD DETAILS

General reagent information

All starting materials were purchased from Sigma-Aldrich and used as received without further purification.

Synthesis of A_2PbX_4 compounds

Polycrystalline powder samples of $(CHA)_2PbX_4$ and $(CPA)_2PbX_4$ were obtained by mixture of stoichiometric amounts of cyclohexylamine or cyclopentylamine with the correspondent PbX_2 lead halide and HX acid. Amounts of starting materials employed in the synthesis of $(CHA)_2PbX_4$ and $(CPA)_2PbX_4$ compounds were the followings: $(CHA)_2PbBr_4$ mixture of 0.81 mL of CHA, 1.25 g of $PbBr_2$ and 20 mL of HBr; $(CHA)_2PbCl_4$ mixture of 1.02 mL of CHA, 1.16 g of $PbCl_2$ and 20 mL of HCl; $(CPA)_2PbBr_4$ mixture of 0.74 mL of CPA, 1.36 g of $PbBr_2$ and 20 mL of HBr and $(CPA)_2PbCl_4$ mixture of 0.91 mL of CPA, 1.24 g of $PbCl_2$ and 20 mL of HCl. The obtained solutions were heated up to 170°C for 10 h and cooled down to room temperature along 72 h. Finally, the obtained polycrystalline powder samples were isolated by filtration, washed several times with diethyl ether and dried under vacuum.

Powder X-Ray diffraction

Powder X-ray diffraction (PXRD) patterns of the obtained polycrystalline powders were collected in a laboratory Siemens D-5000 diffractometer using CuK_α radiation at room temperature.

In addition, synchrotron powder X-ray diffraction (SPXRD) patterns were recorded at the BL04-MSPD beamline of the ALBA Synchrotron (Barcelona, Spain) using a wavelength of 0.4124 Å. The wavelength was determined by refining the positions of six individual reflections of a NIST640D silicon standard. Patterns were collected using Mythen position sensitive detector while heating the sample from RT to 475 K. For this purpose, each sample was enclosed in a quartz capillary (inner diameter $\varphi = 0.5$ mm) and in continuous rotation during data collection to improve powder averaging. The working temperature was set using an FMB Oxford hot-air blower. When carrying out these experiments, the $(CHA)_2PbCl_4$ compound was clearly observed to be very sensitive to the high flux of radiation. For this reason, it was impossible to obtain structural information from the collected data of this compound.

LeBail analysis was carried out using the program GSAS (Larson and Von Dreele, 2000) and EXPGUI software (Toby, 2001). It should be noted that we have also tried to do Rietveld refinement of the obtained data, but it was impossible to satisfactorily solve the crystal structures due to strong preferred orientations in the samples, the presence of lead and bromide/chloride with large atomic scattering factor, disorder C and N atoms with low atomic scattering factor and large atomic displacement parameters.

Thermal analysis

Thermogravimetric analysis (TGA) were carried out in a TGA-DTA Thermal Analysis SDT2960 equipment. Approximately 33 mg of powder was heated at a rate of 10 K/min from 300 K to 1200 K for the experiment, using a corundum crucible, under a flow of dry nitrogen.

Differential scanning calorimetric (DSC) analysis were carried out in a TA Instruments MDSC Q-2000 by heating and cooling the samples under a nitrogen atmosphere, during several cycles at 10 K/min from room temperature up to 520 K.

Ultraviolet-visible (UV-Vis) spectroscopy

Optical diffuse-reflectance measurements of polycrystalline powders were performed at room temperature using a Jasco V-650 UV-Visible double-beam spectrophotometer with single monochromators, operating from 200 nm to 800 nm $BaSO_4$ was used as a non-absorbing reflectance reference. The generated reflectance-versus-wavelength data were used to estimate the band-gap of the materials by converting reflectance to absorbance data according to the Kubelka–Munk equation: $F(R) = \alpha = (1-R)^2/2R$, where R is the reflectance data and α are the absorption coefficients.

Emission spectra were measured on a Horiba FluoroMax Plus-P spectrofluorometer equipped with a 150 W ozone-free xenon arc lamp and a R928P photon-counting emission detector, as well as a photodiode reference detector for monitoring lamp output. Samples were excited using a 150 W Xenon arc lamp at 365 nm and their emission was measured from 370 nm to 800 nm.

The chromaticity coordinates were calculated using the ColorCalculator by OSRAM Sylvania, Inc and plotted using the 1931 color space chromaticity diagram.

Time-resolved photoluminescence decays were measured on a Horiba FluoroMax Plus-P spectrofluorometer working in the phosphorescence lifetime Spectroscopy mode, using 365 nm as an excitation wavelength.

Temperature-dependent luminescence measurements were performed with a cryo-stage, Linkam THMS-LNP95 cooling system.

Dielectric properties

The complex dielectric permittivity ($\varepsilon_r = \varepsilon'_r - i\varepsilon''_r$) of cold-press pelletized samples was measured as a function of frequency and temperature with a parallel-plate capacitor coupled to a Solartron1260A Impedance/Gain-Phase Analyzer, capable to measure in the frequency range from 1 Hz up to 1 MHz using an amplitude of 1 V. The capacitor was mounted in a Janis SVT200T cryostat refrigerated with liquid nitrogen and with a Lakeshore 332 incorporated to control the temperature from 100 K up to 400 K. The data were collected on heating, and before carrying out the measurement the pellets were maintained at each temperature for 2 min, so as to allow them to reach thermal equilibrium. Pelletized samples, with an area of approximately 133 mm^2 and a thickness of approximately 1 mm, were prepared by cold-press to fit into the capacitor. Gold was previously sputtered on the surfaces of the pelletized samples to ensure a good electrical contact. All the dielectric measurements were carried out in a nitrogen atmosphere, performing several cycles of vacuum and nitrogen gas to ensure a sample environment free of water.

QUANTIFICATION AND STATISTICAL ANALYSIS

The study does not include statistical analysis or quantification.

ADDITIONAL RESOURCES

The study has not generated or contributed to a new website/forum or if it is not part of a clinical trial.